

Soft Robotic Snake Locomotion: Modeling and Experimental Assessment

Dimuthu D. K. Arachchige¹, Yue Chen², and Isuru S. Godage¹

Abstract—Snakes are a remarkable evolutionary success story. Numerous snake-inspired robots have been proposed over the years. Soft robotic snakes (SRS), with their continuous and smooth bending capability, can better mimic their biological counterparts' unique characteristics. Prior SRSs are limited to planar operation with a limited number of planar gaits. We propose a novel SRS with spatial bending ability and investigate snake locomotion gaits beyond the planar gaits of the state-of-the-art systems. We derive a complete floating-base kinematic model of the SRS and use the model to derive joint-space trajectories for serpentine and inward/outward rolling locomotion gaits. These gaits are experimentally validated under varying frequency and amplitude of gait cycles. The results qualitatively and quantitatively validate the proposed SRSs' ability to leverage spatial bending to achieve locomotion gaits not possible with current SRS designs.

I. INTRODUCTION

Snakes are highly capable animals with a wide range of habitats, including hostile deserts, dense tropical forests, and uninhabitable marshes. One key feature that makes snakes unique in their ability to navigate in different terrains using various locomotion gaits is supported by their long, high degrees of freedom (DoF) slender bodies. The body's continuous and smooth bending structure enables snakes to overcome numerous environmental challenges such as climbing, swimming despite having no sophisticated appendages such as limbs. Their high DoF body can generate a range of locomotion gaits such as lateral undulation, rectilinear movement, sidewinding, concertina movement. Snake-like robots can harness this traversability in different and challenging terrains in applications such as inspection tasks, reconnaissance, search, and rescue operations. Their small cross-section to length ratio allows them to gain access through tight spaces, little narrow openings (i.e., sewage lines), and perform assigned operations. Robotics have developed various snake robot prototypes [1]–[9] to meet the aforementioned application challenges.

A. Prior Work

Prior work on snake robots mainly evolved with modular rigid robots [1], [4]–[6]. Rigid robotic snakes (RRS) use jointed rigid links to achieve bending motion and generate

¹Dimuthu D. K. Arachchige and Isuru S. Godage are with the Robotics and Medical Engineering Laboratory, School of Computing, DePaul University, Chicago, IL, 60604. darachch@depaul.edu. ²Yue Chen is with the Department of Mechanical Engineering, University of Arkansas Fayetteville, AR, 72701.

This work supported in part by the National Science Foundation grants IIS-1718755, IIS-2008797, IIS-2048142, UARK Chancellor's Fund for Innovation and Collaboration, and DePaul University Academic Initiative Grant 602034.

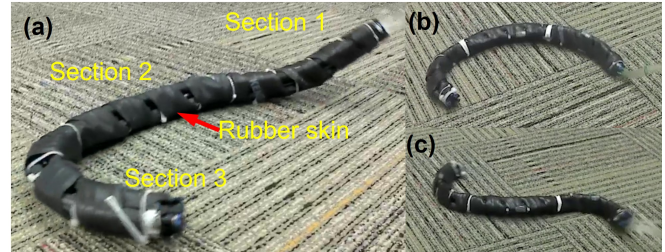


Fig. 1: The proposed (a) Soft robotic snake (SRS) prototype replicating (b) rolling locomotion, and (c) serpentine locomotion.

locomotion. RRS, with few rigid links, limits the robot from achieving the smooth bending observed in snakes and, therefore, can affect locomotion. On the other hand, soft robotic snakes (SRS), constructed mainly from fluidic muscle actuator-powered bodies, can better leverage smooth bending to imitate snake body movements. However, the latest SRS prototypes are limited to planar bending deformation, limiting the number of gaits they can demonstrate [10]. In addition, snakes use differential friction property of their skin to generate locomotion in planar gaits such as serpentine gait [11]. Without such friction profiles in SRS, it is challenging to propel robots solely via planar locomotion gaits. Thus, current SRS rely on wheels to circumvent uniform friction and generate locomotion [9], [10]. Similarly, the SRS reported in [8], [12], [13] use wheels to generate serpentine locomotion. The SRS presented in [14] and [15] is self-contained with integrated sensing and feedback control. It improves the accuracy of dynamic undulatory locomotion. Branyan et al. in [16] have focused on snakeskin properties to improve locomotion. We posit that it is essential to exploit the out-of-plane deformation (spatial bending) to replicate locomotion gaits such as rolling and sidewinding that rely less on anisotropic friction. We propose a novel SRS with spatial bending capabilities to address some of these limitations in state-of-the-art designs.

B. Contribution

The main contributions of this work are (a) propose a novel SRS with spatial bending capability, (b) derive complete floating base kinematic model, (c) derive joint-space trajectories of serpentine, inward rolling, and outward rolling snake locomotion gaits, (d) experimentally validate the said locomotion gaits for a range of pressure-frequency combinations on the propose SRS, (e) demonstrate the need for spatial bending to overcome the limitations of friction anisotropy present in practical SRS. The experimental results show that SRS can successfully track the spatial shape trajectories for

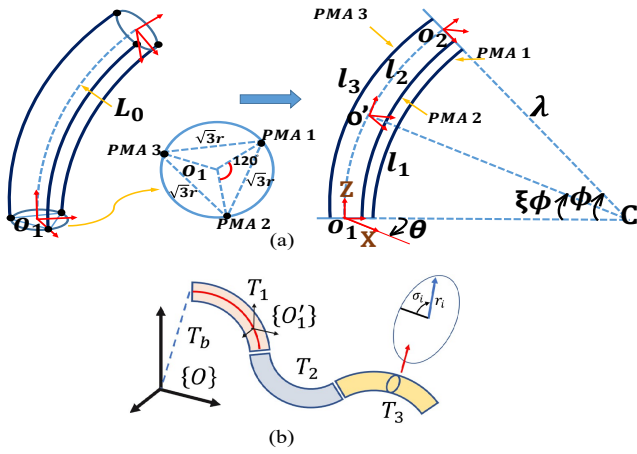


Fig. 2: A schematic of a single section and a schematic of the SRS.

the rolling gaits very well. This SRS utilizes spatial bending capability and demonstrates meaningful locomotion (using inward/outward rolling gait) without wheels. The locomotion is supported by the friction forces generated solely through snake skin-ground interactions.

II. SYSTEM MODEL

A. Prototype Description

Fig. 1 shows the prototype of the proposed SRS. It is made of three serially attached soft bending modules (or sections). They are powered by McKibben type extending mode pneumatic muscle actuators (PMA) [17]. These actuators proportionally extend the body to supplied pneumatic pressure up to 4 bars. In a single soft module, 3 PMAs are assembled at $\frac{\pi}{3}$ separation from each other to ensure symmetric spatial bending and facilitate room to route pneumatic supply lines within the module for a streamlined physical profile required for a slender snake-like body. Each PMA has an unactuated length, $L_{i0}=0.15$ m, and can extend by 0.065 m at 4 bar pressure. Rigid 3D printed mounting frames (made of ABS thermoplastic) are used to mount PMAs at $r_i=0.0125$ m from the centerline of soft modules (Fig. 1). Similarly, laser-cut plastic constrainer plates of r_i and 0.0025 m thickness are used along the soft modules' length to maintain PMAs parallel to soft modules' central axis with a r_i clearance from the central axis. The constrainer plates also provide structural strength for this long and slender SRS to maintain its structural integrity during locomotion and generate reaction forces required for locomotion. All actuators are bundled within the soft module as a single unit, similar to the continuum sections reported in [18]. The pressure differential among PMAs of a soft module causes the module to bend in any direction or extend axially. Thus we can control the bends synchronously in order to generate various types of robot locomotion gaits. Soft modules are then connected via the mounting frames at a $\frac{\pi}{3}$ offset to each other to create the SRS (Fig. 1). Finally, the SRS is wrapped with rubber skin, and without the pneumatic supply lines, it weighs close to 0.3 kg.

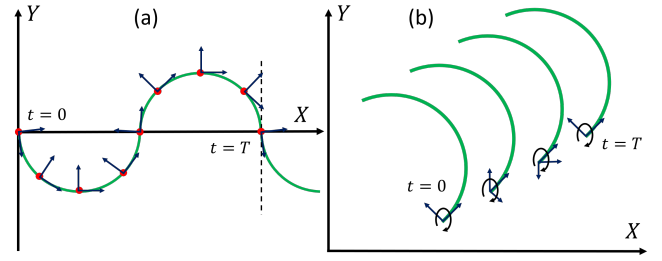


Fig. 3: Trajectory sampling at different time instances within a gait cycle for (a) serpentine gait and (b) outward rolling gait.

B. Kinematic Model

Consider the schematic of any i^{th} module ($i \in \{1, 2, 3\}$) of the SRS, as shown in Fig. 2-a. It depicts three mechanically identical variable length actuators (i.e., PMAs) with an unactuated length $L_{i0} \in \mathbb{R}$ and length change $l_{ij}(t) \in \mathbb{R}$, where $j \in \{1, 2, 3\}$ is the actuator index, and t is the time. Hence, the length of an actuator at any time is $L_{ij} = L_{i0} + l_{ij}(t)$. The kinematic model of the proposed SRS can be formulated by extending the modal kinematics proposed by Godage et al. in [19]. Let the joint-space vector of any i^{th} soft robot module be $q_i = [l_{i1}(t), l_{i2}(t), l_{i3}(t)]^T$. Utilizing the results from [19], we can derive the homogeneous transformation matrix (HTM) at any point along the neutral axis of the i^{th} soft module, $\mathbf{T}_i \in \mathbb{SE}^3$, as

$$\mathbf{T}_i(q_i, \xi_i) = \begin{bmatrix} \mathbf{R}_i(q_i, \xi_i) & p_i(q_i, \xi_i) \\ 0 & 1 \end{bmatrix} \begin{bmatrix} \mathbf{R}_z(\sigma_i) & p_x(\delta_i) \\ 0 & 1 \end{bmatrix} \quad (1)$$

where $\mathbf{R}_i \in \mathbb{SO}^3$ is the rotational matrix, $p_i \in \mathbb{R}^3$ is the position vector $\xi_i \in [0, 1]$ is a scalar to define points along the soft module with 0, and 1 denotes the base and the tip, and I_3 is the rank 3 identity matrix. In addition to the previous results in [19], note that we introduce two HTMs with $\mathbf{R}_z \in \mathbb{SO}^3$ is the rotation matrix about the $+Z$ axis, and $p_x \in \mathbb{R}^3$ is the position offset along the $+Z$ of O'_i where $\sigma_i \in [0, 2\pi]$.

Utilizing (1) with a floating-base coordinate system, $\mathbf{T}_b \in \mathbb{SE}^3$, the complete kinematic model along the body of the snake robot (Fig. 2-b) is given by

$$\begin{aligned} \mathbf{T}(q_b, q, \xi) &= \mathbf{T}_b(q_b) \prod_{i=1}^3 \mathbf{T}_i(q_i, \xi_i) \\ &= \begin{bmatrix} \mathbf{R}(q_b, q, \xi) & p(q_b, q, \xi) \\ 0 & 1 \end{bmatrix} \end{aligned} \quad (2)$$

where $q_b = [x_b, y_b, z_b, \alpha, \beta, \gamma]$ are the parameters of the floating coordinate system with $[x_b, y_b, z_b]$ denote the translation and $[\alpha, \beta, \gamma]$ denote the XYZ Euler angle offset of the base of module 1, i.e., the origin of the robot coordinate frame, with respect to $\{O\}$. The composite vector $q = [q_1, q_2, q_3] \in \mathbb{R}^9$ and $\xi = [0, 3] \in \mathbb{R}$.

III. TRAJECTORY GENERATION

In this work, we consider serpentine, inward rolling, and outward rolling locomotion gaits, which are cyclic in nature. We can mathematically model these gaits associated with different locomotion gaits to generate the taskspace

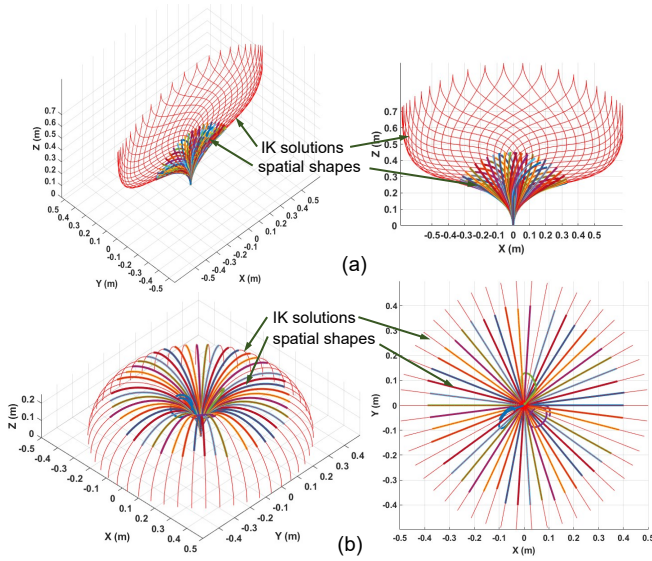


Fig. 4: Trajectory curves in the robot coordinate frame: (a) Serpentine locomotion, (b) Rolling locomotion.

trajectories thereof. Fig. 3 shows the taskspace trajectories of serpentine and outward rolling locomotion. The serpentine curve is given by

$$\begin{aligned} x(s) &= \int_0^s \cos(a \cos(b\sigma) + c\sigma) d\sigma \\ y(s) &= \int_0^s \sin(a \cos(b\sigma) + c\sigma) d\sigma \end{aligned} \quad (3)$$

where $a = -\frac{pi}{4}$, $b = \frac{pi}{4}$, $c = 0$, and $z(s) = 0$.

The rolling gait can be modeled as a mathematical curve – in this case, the displacement of a circular arc with radius r_R , in the rolling gait. One cycle of the rolling gait is defined as the rotation of the curve about its longitudinal axis (Z-axis in the robot coordinate frame), and the robot displacement on the X-Y plane is due to the thickness of the robot that can be derived as $2\pi r_i$, where r_i is the radii of soft modules. From one period of a gait, we derive spatial shapes from the curve at different time intervals within one locomotion cycle to obtain different spatial shapes resembling the snake shape at each of those instances. Similarly, Fig. 3 shows the progression of the serpentine gait and inward rolling gait in one cycle. The dots along the serpentine curve, shown in Fig. 3-a denote the robot origin of the robot coordinate frame at the sampling time instances. Similarly, Fig. 3-b shows the rolling locomotion progression at different time instances. Next, we map these spatial shape trajectories to the joint-space trajectories of the SRS. The kinematic model we derived in Sec. II-B, given by (2) has a floating base coordinate that denotes the origin of the SRS with respect to the inertial frame. However, the floating DoFs are redundant for generating the bending shape of the robot. We follow the steps outlined below to identify the shapes and project those shapes to the SRS's coordinate system.

From the progression of the locomotion gait at different times within a period, we define the curves' origin at those points (Fig. 3). Without losing generality, consider any n^{th}

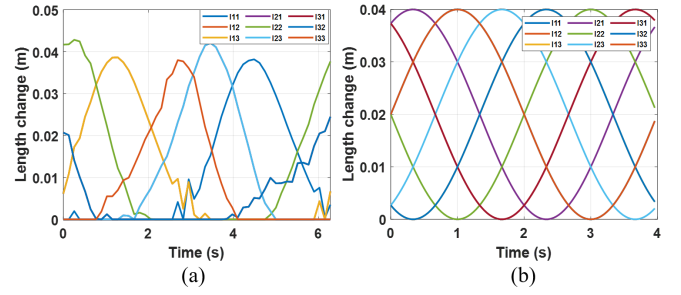


Fig. 5: Joint-space (length change of each PMA) trajectories of (a) serpentine gait, (b) rolling gait for a single cycle.

point along the curve. We derive a local coordinate frame with respect to the inertial frame at those points. For instance, Fig. 3-a shows how we derive coordinate frames at locations shown as dots. For the serpentine curve, a tangential line to the curve and a line normal to this tangential line is defined as the unit vectors along the local Y and X axes as \vec{e}_X and \vec{e}_Y respectively. The unit vector of the Z-axis is derived from $\vec{e}_X \times \vec{e}_Y$. This information and the position vector of the location under consideration are then used to derive the HTM at that point relative to the inertial frame. In the case of the rolling gait, due to the curve's rotation about its longitudinal axis, the robot coordinate frame is 3D (Fig. 3-b).

Utilizing these HTMs at each instance, we project the related mathematical curve onto the body coordinate frame. This step is repeated for all the subsequent taskspace curve shapes within a gait cycle. Figs. 4-(a) and (b) illustrate the spatial shapes for serpentine and rolling motions projected onto the robot coordinate frame, respectively. Next, we derive the joint-space variables for each spatial shape, such that map the SRS shape to the curves under consideration. To that end, we formulate shape matching as an optimization problem. Utilizing the kinematic model given in (2), we define 31 uniformly distributed points (10 points per soft module) along the SRS neutral axis by sampling ξ . Then we define the cost function given by

$$f_{cost} = \sum_{k=1}^{31} \|p(0, q, \xi_k) - f_{gait}(s)\| + \sum_{i,j \in \{1,2,3\}} l_{ij}^2 \quad (4)$$

where $0 \leq \xi_k \leq 3$ and f_{gait} is the locomotion gait shape to which the SRS is fitted, and s defines the points along f_{gait} .

The SRS concerned here are constructed from three extensible soft modules, and the latter term of (4) ensures that the optimization solution has the least total extension. This ensures the joint-space trajectories stay smooth without unnecessary length changes between solutions. We use Matlab's global constrained optimization routine to optimize the SRS shape and save the joint-space solution. Fig. 4 shows the matched SRS shapes in thick lines. There are instances where the optimization failed. However, this has little effect on the overall joint-space trajectory due to the dense sampling of gait cycles. One may rerun the optimization routine with different initial conditions to obtain a solution. We repeat the process for all the spatial mathematical curves associated with each instance of the locomotion gaits. Fig. 5 shows the

joint-space trajectories for serpentine and rolling snake locomotion gait for several cycles. Note that the outward rolling trajectory is the reverse of the inward rolling trajectory. The cycle frequency of these gaits can be scaled by adjusting the cycle period. Similarly, the change of amplitude of the joint-space values results in more bending. In the case of rolling locomotion, this means a reduced r_R , i.e., rolling arc radius, whereas it increases the serpentine gait's amplitude.

IV. EXPERIMENTAL VALIDATION

A. Experimental Setup

Fig. 6a shows the overall experimental setup of the snake robot. It consists of an input pressure source, pressure controllers, pressure command interface, and the SRS. The setup's input pressure is a constant 8 bar pressure supplied by an air compressor. The pressure to the PMAs is controlled by SMC ITV3000 series digital proportional pressure regulators and supplied via 4 mm diameter tubes. The commands to the pressure regulators are generated through a Matlab Simulink Desktop Realtime model and interfaced via a 0-10 V voltage signal using a National Instrument DAQ card. The SRS is tested on a carpeted floor, as shown in Fig. 7.

B. Testing Procedure

The SRS prototype is tested for three snake locomotion gaits; serpentine, inward rolling, and outward rolling presented in Sec. III. The joint-space trajectories given in Fig. 4 depict the length changes of PMAs. To control the pressure to PMAs, we first need to establish a mapping between the PMA pressure input and the resulting length changes. We note that the SRS needs to work with relatively fast movements to generate highly dynamic locomotion trajectories. Therefore, an empirical and static length-to-pressure mapping-based approach may result in low accuracy. We examined the PMA length changes under for 1 Hz rectified triangular wave and found that $P_{ij} = 100l_{ij}$ provides acceptable results where P_{ij} is the pressure in bars to control the joint variable l_{ij} (i.e., length change). We tested the gait trajectories for 15 s in pressure amplitudes {1,2,3,4} bars and frequencies {0.25,0.5,0.75,1.0} Hz combinations, totaling 16 experiments per gait type. The SRS motion is captured using a fixed camera station. We applied image perspective projection [20] to track the robot movements.

C. Serpentine Motion

Fig. 7-a shows a chronological shape change of the robot for the serpentine motion at 4 bar pressure amplitude and 0.25 Hz frequency. We found that this combination replicates the best serpentine patterns. Fig. 8:A-C show how the proposed SRS behaves during serpentine motion at 2 bar-0.25 Hz, 4 bar-0.25 Hz, and 4 bar-1.00 Hz, pressure-frequency combinations. Refer to the accompanying multimedia submission for the videos of the experiments. Further, we did not observe any meaningful serpentine locomotion in the axial direction, as shown in Fig. 8:A-C. Further, it is discovered from the numbers indicated in Table I under the traveling velocity of the serpentine gait. Here, the robot

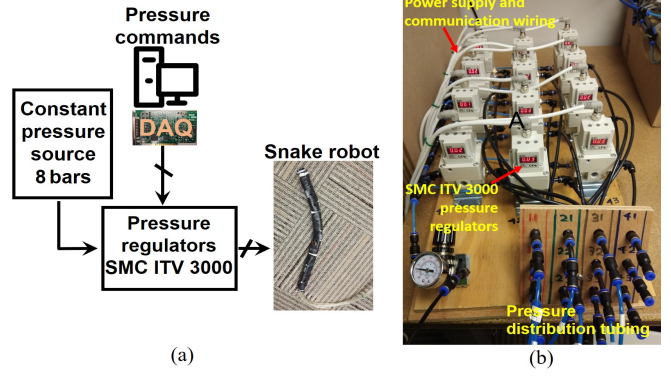


Fig. 6: (a) Schematic diagram of the robot experimental setup, (b) Pressure regulator assembly that control the length change of PMAs.

wobbles around without making any progress. This is a common problem with snake robots [16]. It is mainly due to insufficient friction difference in the robot skin in normal and tangential directions. In the real world, snakes have different friction coefficients in these directions. In our robot, the skin is made of a rubber surface, resulting in the same friction coefficient in all directions. Therefore the robot cannot generate a forward propagation force in the axial direction. As expected, it does not result in any forward locomotion with serpentine patterns. This is one of the main reasons why the prior work involving planer SRS [7]–[10], [12]–[15] use wheels. The wheels generate low friction in the axial direction and high friction in the normal direction.

D. Inward Rolling Motion

Fig. 7-b shows a chronological shape change of the robot during inward rolling at 4 bar actuation pressure and 1.0 Hz frequency, which stands as the best combination to illustrate inward rolling locomotion at the highest velocity. Figs. 8:D-F shows how the robot behaves during inward rolling at 2 bar-0.25 Hz, 3 bar-0.50 Hz, and 4 bar-1.00 Hz, pressure-frequency combinations. We observed that the robot could successfully replicate inward rolling locomotion at all pressure and frequency combinations except at a pressure as low as 1 bar. At 2 bar, when the moving frequency was high as 1 Hz, the robot occasionally flipped back in the opposite direction. Further, the robot shows a low bending curvature at higher actuation pressure and frequency combinations. This is mainly due to air pressure not reaching the PMAs in realtime through long pneumatic lines. In both inward and outward rolling gaits, the highest traveling velocity is observed when the applied pressure-frequency combination is at its maximum value, i.e., 4 bar-1.00 Hz (Fig. 8:F-I and Table I). The SRS's rolling locomotion exploits 3D bending to rotate about its longitudinal axis, and this is the first time rolling locomotion is achieved by the SRS. Unlike serpentine gait, we demonstrate that SRS locomote successfully via rolling gaits. Here, the friction is applied in the rolling direction and supports rolling without interference, similar to moving a wide and continuous wheel. We observed similar performance in reverse rolling (Sec. IV-E).

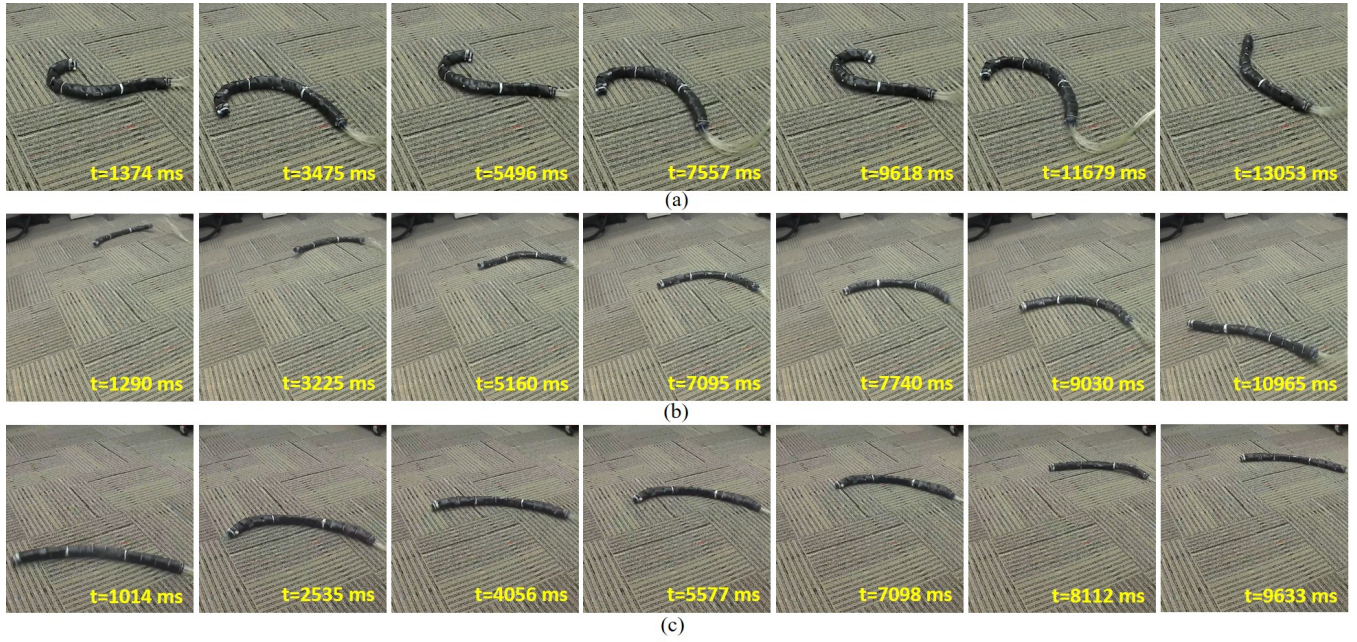


Fig. 7: (a) Serpentine gait at 4 bar-0.25 Hz, (b) Inward rolling and (c) Outward rolling gaits at 4 bar-1.00 Hz pressure-frequency combinations.

TABLE I: Traveling velocity of robot locomotion gaits. Velocity is computed by dividing the mean of the X and Y displacements by the experiment time.

Pressure amplitude (bar)	Frequency (Hz)	Travelling velocity (cm/s)					
		Serpentine motion		Inward rolling		Outward rolling	
		v_x	v_y	v_x	v_y	v_x	v_y
1.0	0.25	0.00	0.00	0.00	0.00	0.00	0.00
	0.50	0.00	0.00	0.00	0.00	0.00	0.00
	0.75	0.00	0.00	0.00	0.00	0.00	0.00
	1.00	0.00	0.00	0.00	0.00	0.00	0.00
2.0	0.25	0.07	0.13	1.14	2.21	0.44	2.20
	0.50	0.12	0.16	2.11	3.21	1.29	2.02
	0.75	0.14	0.21	2.98	3.99	2.15	1.82
	1.00	0.08	0.14	3.43	4.32	3.01	1.48
3.0	0.25	0.28	0.43	3.99	4.87	3.33	2.08
	0.50	0.49	0.65	4.05	5.72	5.69	0.12
	0.75	0.59	0.71	5.16	5.89	4.21	2.19
	1.00	0.28	0.55	5.23	7.89	4.89	1.91
4.0	0.25	0.76	0.36	3.12	7.55	4.03	3.91
	0.50	0.63	0.28	4.16	9.11	5.79	2.78
	0.75	0.21	0.27	4.98	9.67	6.39	4.55
	1.00	0.09	0.18	5.61	10.11	6.56	6.75

E. Outward Rolling Motion

Fig. 7-c shows a chronological shape change of the robot during outward rolling motion at 4 bar actuation pressure and 1.0 Hz frequency. We found that this is the best combination to illustrate outward rolling locomotion at maximum velocity. Fig. 8:G-I show how the robot behaves during inward rolling at 2 bar-0.25 Hz, 3 bar-0.50 Hz, and 4 bar-1.00 Hz, pressure-frequency combinations. Table I shows the calculated traveling velocity of all three locomotion gaits based on image tracking results in Fig. 8. Here, the robot performs outward rolling towards opposite to its curve opening. The robot cannot perform very well as much as in the other direction. The friction is applied opposite the rolling direction, and the friction force interferes with the generated rolling thrust. This

is proved by relatively low velocities recorded in Table I.

F. Discussion

The tracking results in Fig. 8 show that the SRS replicates the three locomotion gaits very well. When the actuation pressure is low at 1 bar regardless of frequency or the locomotion gait type, the robot showed almost no movements. This is mainly due to the associated 1.0-bar deadzone present in PMAs where no length change was observed and, therefore, no bending. Starting from 1.5 bar pressure, the SRS starts to replicate all locomotion gaits well. The best replication of serpentine gait is observed at 4 bar-0.25 Hz pressure-frequency combination, as presented in Fig. 7-a. At 2 bar pressure and 0.25-0.50 Hz low-frequency combinations, the SRS shows considerably slow serpentine patterns. At low frequencies, when pressure increases from 2 to 4 bar, the serpentine pattern improves. However, at higher frequencies, the pressure amplitude distorts the gait pattern replication, as presented in Fig. 8-C. This is due to these fast pressure changes not reaching PMAs in realtime through long pneumatic lines. Therefore the caused propagation delay interferes with replication patterns.

V. CONCLUSIONS

Snakes are highly capable animals with a unique ability to navigate challenging terrains using different locomotion gaits. We proposed an SRS that can replicate various snake locomotion gaits. We derived a full floating base kinematic model. We derived the joint-space trajectories for three gait types, namely serpentine, inward, and outward rolling motion, via an optimization approach. We experimentally tested the SRS for serpentine and rolling snake locomotion. The SRS successfully tracked the spatial shape trajectories

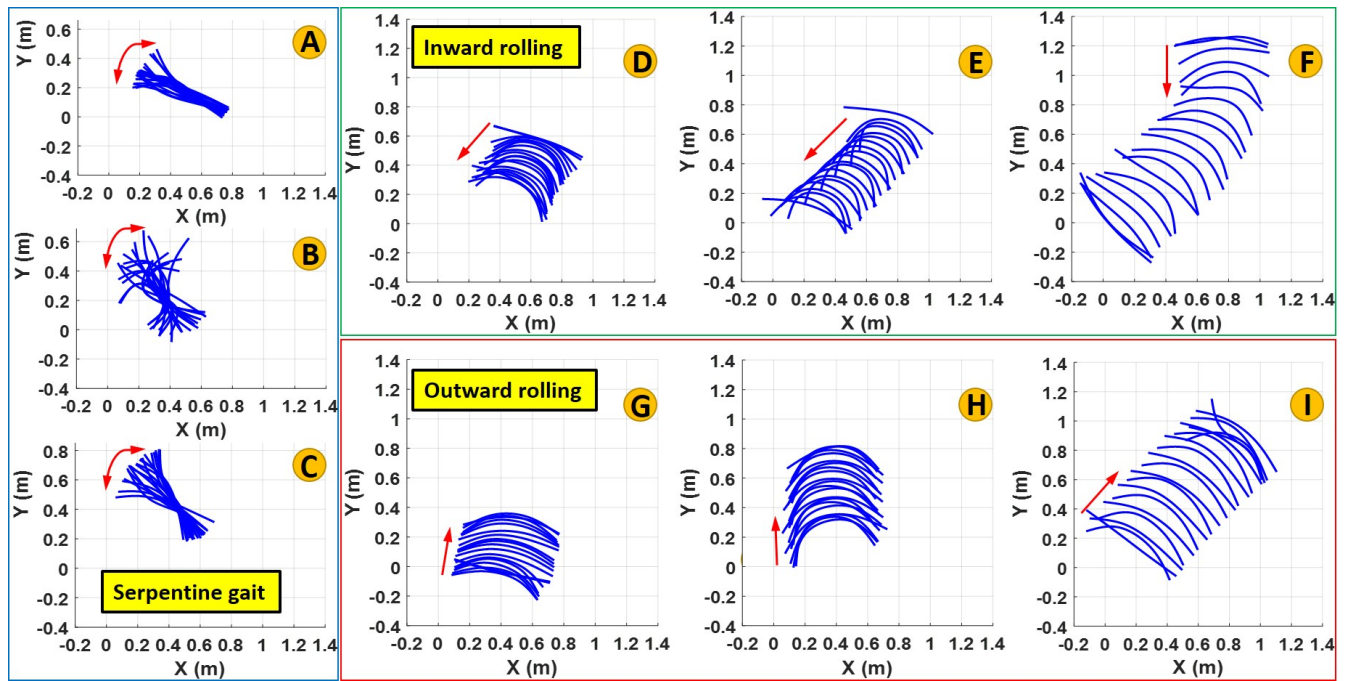


Fig. 8: Tracking of robot movement for serpentine gait at (A) 2 bar-0.25 Hz, (B) 4 bar-0.25 Hz, and (C) 4 bar-1.00 Hz pressure-frequency combinations; Inward rolling gait at (D) 2 bar-0.25 Hz, (E) 3 bar-0.50 Hz, and (F) 4 bar-1.00 Hz pressure-frequency combinations; and Outward rolling gait at (G) 2 bar-0.25 Hz, (H) 3 bar-0.50 Hz, and (I) 4 bar-1.00 Hz pressure-frequency combinations.

for all the gaits at high-pressure amplitudes and low frequencies as expected. Due to the uniform friction coefficient present in both longitudinal and normal motion directions, no meaningful displacement is observed in SRS for the serpentine gait. In contrast, inward and outward rolling gait successfully achieved locomotion. This is the first time that the rolling locomotion is demonstrated in an SRS.

REFERENCES

- [1] S. Hirose and M. Mori, "Biologically inspired snake-like robots," in *2004 IEEE International Conference on Robotics and Biomimetics*. IEEE, 2004, pp. 1–7.
- [2] S. Hirose and H. Yamada, "Snake-like robots [tutorial]," *IEEE Robotics & Automation Magazine*, vol. 16, no. 1, pp. 88–98, 2009.
- [3] C. Wright, A. Johnson, A. Peck, Z. McCord, A. Naaktgeboren, P. Gianfortoni, M. Gonzalez-Rivero, R. Hatton, and H. Choset, "Design of a modular snake robot," in *2007 IEEE/RSJ International Conference on Intelligent Robots and Systems*. IEEE, 2007, pp. 2609–2614.
- [4] C. Wright, A. Buchan, B. Brown, J. Geist, M. Schwerin, D. Rollinson, M. Tesch, and H. Choset, "Design and architecture of the unified modular snake robot," in *2012 IEEE International Conference on Robotics and Automation*. IEEE, 2012, pp. 4347–4354.
- [5] A. A. Transeth, R. I. Leine, C. Glocker, and K. Y. Pettersen, "3-d snake robot motion: nonsmooth modeling, simulations, and experiments," *IEEE transactions on robotics*, vol. 24, no. 2, pp. 361–376, 2008.
- [6] A. Crespi and A. J. Ijspeert, "Online optimization of swimming and crawling in an amphibious snake robot," *IEEE Transactions on Robotics*, vol. 24, no. 1, pp. 75–87, 2008.
- [7] M. Luo, W. Tao, F. Chen, T. K. Khuu, S. Ozel, and C. D. Onal, "Design improvements and dynamic characterization on fluidic elastomer actuators for a soft robotic snake," in *2014 IEEE International Conference on Technologies for Practical Robot Applications (TePRA)*. IEEE, 2014, pp. 1–6.
- [8] C. D. Onal and D. Rus, "Autonomous undulatory serpentine locomotion utilizing body dynamics of a fluidic soft robot," *Bioinspiration & biomimetics*, vol. 8, no. 2, p. 026003, 2013.
- [9] Y. Qin, Z. Wan, Y. Sun, E. H. Skorina, M. Luo, and C. D. Onal, "Design, fabrication and experimental analysis of a 3-d soft robotic snake," in *2018 IEEE International Conference on Soft Robotics (RoboSoft)*. IEEE, 2018, pp. 77–82.
- [10] M. Luo, R. Yan, Z. Wan, Y. Qin, J. Santoso, E. H. Skorina, and C. D. Onal, "Orisnake: Design, fabrication, and experimental analysis of a 3-d origami snake robot," *IEEE Robotics and Automation Letters*, vol. 3, no. 3, pp. 1993–1999, 2018.
- [11] J. Hazel, M. Stone, M. Grace, and V. Tsukruk, "Nanoscale design of snake skin for reptation locomotions via friction anisotropy," *Journal of biomechanics*, vol. 32, no. 5, pp. 477–484, 1999.
- [12] M. Luo, M. Agheli, and C. D. Onal, "Theoretical modeling and experimental analysis of a pressure-operated soft robotic snake," *Soft Robotics*, vol. 1, no. 2, pp. 136–146, 2014.
- [13] M. Luo, Y. Pan, W. Tao, F. Chen, E. H. Skorina, and C. D. Onal, "Refined theoretical modeling of a new-generation pressure-operated soft snake," in *International Design Engineering Technical Conferences and Computers and Information in Engineering Conference*, vol. 57144. American Society of Mechanical Engineers, 2015, p. V05CT08A023.
- [14] M. Luo, Y. Pan, E. H. Skorina, W. Tao, F. Chen, S. Ozel, and C. D. Onal, "Slithering towards autonomy: a self-contained soft robotic snake platform with integrated curvature sensing," *Bioinspiration & biomimetics*, vol. 10, no. 5, p. 055001, 2015.
- [15] M. Luo, E. H. Skorina, W. Tao, F. Chen, S. Ozel, Y. Sun, and C. D. Onal, "Toward modular soft robotics: Proprioceptive curvature sensing and sliding-mode control of soft bidirectional bending modules," *Soft robotics*, vol. 4, no. 2, pp. 117–125, 2017.
- [16] C. Branyan, R. L. Hatton, and Y. Mengüç, "Snake-inspired kirigami skin for lateral undulation of a soft snake robot," *IEEE Robotics and Automation Letters*, vol. 5, no. 2, pp. 1728–1733, 2020.
- [17] I. S. Godage, D. T. Branson, E. Guglielmino, and D. G. Caldwell, "Pneumatic muscle actuated continuum arms: Modelling and experimental assessment," in *2012 IEEE International Conference on Robotics and Automation*. IEEE, 2012, pp. 4980–4985.
- [18] I. S. Godage, G. A. Medrano-Cerda, D. T. Branson, E. Guglielmino, and D. G. Caldwell, "Dynamics for variable length multisection continuum arms," *The International Journal of Robotics Research*, vol. 35, no. 6, pp. 695–722, 2016.
- [19] —, "Modal kinematics for multisection continuum arms," *Bioinspiration & biomimetics*, vol. 10, no. 3, p. 035002, 2015.
- [20] T. Ohta, K. Maenobu, and T. Sakai, "Obtaining surface orientation from texels under perspective projection," in *International Joint Conference on Artificial Intelligence (IJCAI)*, vol. 81, 1981, pp. 746–751.